CONFIDENTIAL

Copy 194
RM L55G29

NACA RM L55G29

TECH LIBRARY KAFB, NM
0144114

TECHNICAL LIBRARY
HOLLOMAN AIR FORCE BASE
ALAMOGORDO, NEW MEXICO

7636

NACA

RESEARCH MEMORANDUM

FLIGHT INVESTIGATION AT SUPERSONIC MACH NUMBERS OF AN AUTOMATIC ACCELERATION CONTROL MISSILE IN WHICH RATE DAMPING IS OBTAINED FROM A LINEAR ACCELEROMETER PLACED AHEAD OF THE MISSILE CENTER OF GRAVITY

By Ernest C. Seaberg, Royce H. Sproull,
and H. J. E. Reid, Jr.

Langley Aeronautical Laboratory
Langley Field, Va.

CLASSIFIED DOCUMENT

This material contains information affecting the National Defense of the United States within the meaning of the espionage laws, Title 18, U.S.C., Secs. 793 and 794, the transmission or revelation of which in any manner to an unauthorized person is prohibited by law.

NATIONAL ADVISORY COMMITTEE
FOR AERONAUTICS

WASHINGTON
November 8, 1955

CONFIDENTIAL

TECH LIBRARY KAFB, NM
0144114

NATIONAL ADVISORY COMMITTEE FOR AERONAUTICS

RESEARCH MEMORANDUM

FLIGHT INVESTIGATION AT SUPERSONIC MACH NUMBERS OF AN AUTOMATIC ACCELERATION CONTROL MISSILE IN WHICH RATE DAMPING IS OBTAINED FROM A LINEAR ACCELEROMETER PLACED AHEAD OF THE MISSILE CENTER OF GRAVITY

By Ernest C. Seaberg, Royce H. Sproull,
and H. J. E. Reid, Jr.

SUMMARY

The results of a supersonic flight investigation of a roll-stabilized acceleration control missile are presented herein. The Mach number variation was 1.7 to 1.4 for the results presented.

The maneuvers obtained during flight confirm satisfactory control system operation and the system is applicable to some present-day missiles which utilize linear acceleration commands to reduce navigation errors. The control elements used to achieve linear acceleration maneuvers in flight are relatively simple. For example, the effect of integration is obtained in the servo loop simply by combining the servo components with the proper passive resistive-capacitive circuit, and this integrating servo is combined with angular acceleration feedback to provide the equivalent of angular rate feedback.

INTRODUCTION

This presentation is primarily concerned with the results of a rocket-powered flight test of an automatic acceleration control missile. The flight test results are compared with preflight simulation and previous analytical results. The analytical results are based on a study presented in reference 1 in which the dynamics of a rate gyroscope was incorporated in the inner feedback loop to provide additional damping. In the results of reference 1, it was also suggested that with the use of an integrating servo, angular rate damping augmentation could be obtained from a linear accelerometer displaced ahead of the missile center of gravity, thereby eliminating the need for a rate gyroscope. In reference 1, it was also shown that insufficient rate damping would be obtained

[redacted]

with one accelerometer since the distance that it could be placed ahead of the center of gravity was limited by the size of the missile. The alternate method suggested was to use two accelerometers, one placed ahead of and one at the center of gravity, and to subtract the accelerometer signals before feeding them to the integrating servo. The use of two accelerometers was employed in the flight-test missile, thereby making the angular rate feedback gain adjustment and the accelerometer gain adjustment independent regardless of the distance between the forward accelerometer and the center of gravity.

Linear acceleration control systems are particularly adapted to homing or guided missiles since flight-path curvature in the proper direction to reduce navigation errors can be attained by dictating acceleration commands to the control system. The idea of rotating the flight-path vector towards a target through the application of linear acceleration commands is not new and is employed in service missiles like the Nike (a description of the Nike control system can be found in ref. 2). However, the control system flight tested herein is characterized by its simplicity since it eliminates the rate gyroscope and utilizes a pneumatic servo system activated by a minimum of electronic components.

The flight-test vehicle used is an all-metal research model of the canard missile type. Physical details of this model are given in reference 3 which discusses the results of a previous flight test conducted for the purpose of obtaining aerodynamic stability derivatives.

SYMBOLS

a_t transverse acceleration, g

a_{t_n} transverse acceleration forces sensed by a linear accelerometer located ahead of the c.g. $\left(a_t + K_l\ddot{\psi}\right)$, g

ψ yaw attitude angle, deg

ϕ bank angle, deg

β sideslip angle, deg

δ vertical canard deflection, deg

δ_f voltage related to δ by the dynamics and gain in the servo feedback loop, volts

δ_i input signal to servo system, volts

ϵ	error signal, $a_{t_i} - a_{t_o}$, volts
K_p	gain constant of servo feedback potentiometer, volts/deg
K_b	static gain of nose accelerometer, volts/g
K_l	conversion factor between angular acceleration and its tangential component, g/deg/sec^2
K_a	forward control loop gain constant, volts/g
K_a'	c.g. accelerometer gain constant
D	differential operator, d/dt
τ	time constant, sec
t	time, sec
ω	angular frequency, radians/sec
g	32.2 ft/sec^2
$\bar{c}$	mean aerodynamic chord, ft
x_{sm}	static margin, ft
M	Mach number
I_X	moment of inertia in roll, slug-ft^2
I_Y	moment of inertia in pitch, slug-ft^2
I_Z	moment of inertia in yaw, slug-ft^2

Dot over a symbol denotes the derivatives with respect to time.

Subscripts:

o	output
i	input

Abbreviations:

db	decibels
c.g.	center of gravity
c.p.	center of pressure
RC	resistive-capacitive
DC	direct current

ACCELERATION CONTROL SYSTEM

Complete System

The general arrangement of the block diagram which completely represents the acceleration control for the purpose of analysis is shown in figure 1(a). This block diagram may be simplified by neglecting the accelerometer dynamics as shown in figure 1(b), where the correspondence between figure 1(a) and figure 1(b) is maintained by equating the forward loop gain constant K_a (fig. 1(b)) to the feedback gains of figure 1(a) in accordance with the relation:

$$K_a = K_a'\left(1 - K_b\right) + K_b$$

Figure 2 is a block diagram which includes the servo signal schematic and also illustrates the servomotor dynamic components.

System Components

Servo system.- A photograph of the servomotor, including the spring and solenoid, is presented in figure 3. This unit consists of a pneumatic ram which is controlled by the solenoid valve. The servomotor is coupled to the yaw canard surfaces and feedback potentiometer through a connecting rod-bellcrank linkage. Some of the significant servomotor physical characteristics are given in table 1.

The servo as illustrated schematically by the mechanical components (solenoid, slide valve, spring, and piston) in figure 2 does not contain position feedback; therefore it has low frequency integrating characteristics. An electropneumatic servo of this type, however, is not an ideal

integrator and it is difficult to control the rate of integration. The addition of a derivative feedback network consisting of the RC circuit shown in figure 2 was found to yield fairly smooth integrating servo operating characteristics in the proper frequency band. This derivative feedback circuit has a transfer function of the form:

$$\frac{\delta_f}{\delta} = \frac{\tau D}{\tau D + 1}$$

Therefore the servo dynamics block of figure 1 represents the dynamics of the electropneumatic servo components combined with the additional dynamics of the derivative feedback circuit and may be redrawn as:

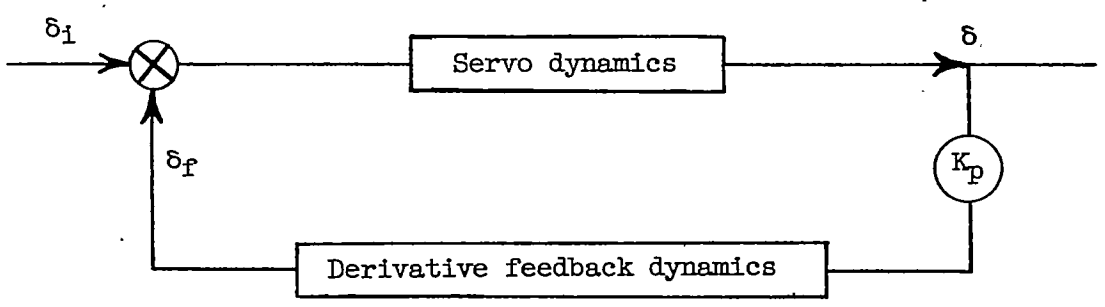

The frequency response δ/δ_i is not easy to measure directly due to the integrating effect between δ and δ_i. Therefore, in order to obtain an approximation of the servo dynamics for preliminary stability analysis, the frequency response of the servo elements with unity position feedback was first measured and is presented in figure 4. This closed loop frequency response was then plotted on a Nichol's chart (see ref. 4). The open loop response of the servo obtained from this Nichol's plot is an approximate representation of the servo dynamics. The frequency response δ/δ_i was then obtained by a graphical combination of the servo dynamics with the derivative feedback dynamics. The δ/δ_i frequency response plot with $\tau = 0.01$ second is shown in figure 5. The value of $\tau = 0.01$ second was chosen as a result of graphical stability checks and subsequent preflight simulation checks of the complete system.

Accelerometers.- A photograph of the type of control system accelerometer used for the present flight test is shown in figure 6. This instrument is a liquid damped, pressurized accelerometer which measures linear acceleration by movement of a spring supported mass. The movement of the mass varies the voltage ratio of a potentiometer in proportion to the applied acceleration and the mass is supported so that the instrument senses acceleration in both the positive and negative direction. The amplitude responses of the nose and c.g. accelerometers for

inputs of ±5g and ±15g obtained from experimental frequency response measurements are presented in figure 7.

Electronics.- The autopilot amplifier (see fig. 2) consists of three stages made up of a two-stage DC summing amplifier working into a single-stage DC power amplifier. The solenoid valve coil is the load of the final stage. Excitation of the accelerometers, follow-up potentiometer, plate voltage and command signal is furnished by the same voltage regulated battery power supply.

PREFLIGHT INVESTIGATION

Physical

The physical characteristics obtained for the acceleration control missile prior to the flight test are given in table 2. In connection with the location of the nose accelerometer, it is noted that the 5.5 foot lever arm between the nose accelerometer and the c.g. placed this instrument as far ahead of the c.g. as was physically possible. Therefore the sensitivity of the accelerometer to the tangential component of yaw angular acceleration was as high as could be attained with this airframe.

Previous Analytical Studies

The analytical results presented herein were obtained directly from the results of reference 1 utilizing a combination of graphical and superposition procedures. The results of reference 1 are based on a system which differs somewhat from the system finally flight tested because in the previous analytical work, the servo and integrator were assumed to be perfect and the dynamics of a rate gyroscope was included in the inner feedback loop. An approximation of the anticipated flight test response is obtained from the data of reference 1 even with these differences, since the oscillating frequency is mainly dependent on the airframe dynamics and the desired damping is obtained in either case by adjustment of the rate feedback loop gain.

The blocks labeled airframe dynamics in figures 1 and 2 represent the airframe transfer functions obtained from the solution of the standard two-degree-of-freedom equations of motion (see ref. 1). For the analytical results and for the preflight simulator predictions of the flight-test response, these transfer functions are as follows:

$$\frac{\ddot{\psi}}{\delta} = \frac{620D(D + 4.5)}{D^2 + 8D + 690}$$

$$\frac{a_{t_o}}{\ddot{\psi}} = \frac{4.35}{D(D + 4.5)}$$

The numerical coefficients are those obtained with $x_{sm} = 0.294\bar{c}$ and are based on sea-level flight conditions at $M = 1.6$ (see ref. 1). These conditions are assumed to approximate the average conditions for the first complete pulsing cycle after model-booster separation based on previous flight-test experience.

Preflight Simulator

Preflight simulation tests of the system illustrated in figure 2 were accomplished through the use of DC computing amplifiers connected to represent the transfer functions of the airframe and accelerometers. Since the undamped natural frequency of the accelerometers was very high compared with the resonant frequency of the system, satisfactory simulation of the accelerometers was obtained with simple gain expressions. An additional linear potentiometer was linked to the servo shaft to provide a voltage proportional to δ as the input to the simulator. The simulator output was connected to the servo system in the same manner as the accelerometers would normally be. In the preflight simulation problem the actual servo, autopilot amplifier, and input programmer were utilized in combination with the electronic analog of the airframe and accelerometers. Through the use of the preflight simulator, the various system gains were adjusted to obtain performance approximately equivalent to the performance obtained analytically. The accelerometer sensitivities to be used for the flight test were then calculated from the simulator settings which yielded the required performance.

The preflight simulator was constructed to simulate a fixed set of flight conditions, thereby making it lightweight and portable. It was therefore possible to take the simulator with the model to the launching site and to obtain a simulator check run before launching to insure that the servo system was operating correctly.

FLIGHT TEST

Model and Booster

A photograph of the model and booster on the launcher is shown in figure 8. This combination has been previously used as the test vehicle in other investigations. References 3 and 5, for example, give the results of previous aerodynamic and roll control flight investigations and contain descriptions of the model and booster aerodynamic configurations.

Flight Description

The model was launched at approximately 60° from the horizontal. Radar was used to obtain the missile flight trajectory and a radiosonde atmospheric calibration was obtained for use in data reduction.

Transverse acceleration was controlled through the action of the vertical canard surfaces. The action of the control system was initiated through step command input voltages dictated by a motor-driven-cam programming device. The pulsing sequence of the programming device is shown in figure 9. These programmed inputs were actually being fed to the control system prior to and during boosted flight with pneumatic supply pressure available at the servo valve. It was necessary, however, to lock the canard control surface at zero degrees during boosted flight for structural reasons. This control surface lock was scheduled to release shortly after model-booster separation through the action of an explosive charge triggered by a switch on the model tail cone.

Roll Control

Automatic roll stabilization was provided through the use of a gyro actuated control linked to wing tip ailerons in the vertical plane. The gyro actuated roll control system and the roll free coupling between model and booster have been previously flight tested and are described in references 3 and 5. The bank angle of the model during the flight test was referenced to the launching condition since the roll control gyro was uncaged prior to launching with the roll control operating during boosted flight. Figure 10 shows the time history of bank angle ϕ obtained during boosted flight and during the subsequent yaw acceleration maneuvers.

INSTRUMENTATION

The model contained a ten-channel telemeter which transmitted measurements of transverse acceleration at the c.g., transverse plus tangential acceleration 5.5 feet ahead of the c.g., angle of sideslip, yaw attitude angle, vertical canard position, servo valve position, programmed input sequence, aileron position, total head pressure and normal acceleration. Angle of sideslip was measured by a standard NACA angle-of-sideslip vane. Yaw attitude measurements were obtained from a calibrated displacement gyro. Although the yaw attitude gyro was uncaged prior to launching, the data presented are referenced to model-booster separation since the few degrees that the model yawed during boosted flight are not relevant to the subsequent yawing maneuvers. Quantitative measurement of servo valve position was not attempted because of the extremely small linear displacements involved. Total

pressure was measured by a standard pressure probe extended from the side of the model nose section.

RESULTS AND DISCUSSION

Analytical Results

The analytical results presented in figure 11 are based on responses obtained from reference 1 for sea-level flight at $M = 1.6$. The sequence of programmed inputs on which figure 11 is based has previously been shown in figure 9. The block diagram shown in the upper part of figure 11 includes the dynamics used for the previous analytical work. The flight conditions on which the analytical predictions are based were chosen because the responses were readily available from reference 1 and these conditions are fairly representative of the actual conditions shortly after missile booster separation.

Preflight Simulator Results

The preflight simulator result obtained at the model launching site prior to the actual flight test is shown in figure 12. The results presented in figure 12 are based on the same flight conditions as the previous analytical results (fig. 11). Although the canard control surfaces were designed with the hinge line located so that the hinge moment would be small for flight at $M = 1.6$, it was decided that it was not entirely negligible and a small spring load (6 in-lb/deg) was imposed on the control surfaces during the simulator tests. The gains $\left(K_b = 0.616 \text{ volt/g}; K_a = 0.136 \text{ volt/g}\right)$ used for the final simulator tests and subsequent flight test were determined from previous system operational checks conducted before the missile was delivered to the launching site. For these operational checks, satisfactory operation of the system was considered to be achieved when the gain adjustment yielded performance approximately equivalent to the performance obtained analytically. The final run made at the launching site and presented as figure 12 was made simply to confirm satisfactory control system operation prior to the flight test.

Figure 13 is a Nichols plot of the open loop frequency response a_{t_o}/ϵ of the system as represented in figure 1(b). This plot is based on the graphical representation of the servo previously shown as figure 5 and on flight conditions identical to those used for the previous analytical and simulation results (figs. 11 and 12). The Nichols plot shown in figure 13 actually represents a confirmation of adequate system stability with the gains adjusted to the values $K_b = 0.616$ volt/g and $K_a = 0.136$ volt/g as determined from the operational check out of the system.

Comparison Between Simulator and Analytical Results

Variation of rate feedback dynamics.- It has been previously mentioned that the dynamics of a rate gyroscope was included in the inner feedback loop for the analytical results presented in figure 11, while for figure 12 the dynamics of the accelerometer is represented by a simple gain expression. Since the amplitude response of the quadratic function which represents the rate gyroscope dynamics is flat for a frequency range equal to approximately 3.5 times the airframe undamped natural frequency, the rate gyroscope dynamics do not appreciably influence the responses shown in figure 11; and therefore a comparison between figures 11 and 12 is not significantly affected by the variation in representation of the rate gyroscope and accelerometer dynamics.

Variation of servo dynamics.- In general a comparison between the responses shown in figures 11 and 12 indicates that the results obtained with the preflight simulator are quite similar to the analytical results. For example, the rise times of the acceleration responses are approximately comparable and only a little less initial overshoot is obtained with the simulator. The main difference between figures 11 and 12, however, is the more oscillatory nature of the simulated transverse acceleration output response in approaching steady state. The differences noted between the theoretical response and the simulator response may be attributed mainly to servo dynamics and nonlinearities, since for the previous analytical study an ideal servo and integrator are assumed; and in the simulation problem, the actual physical servo system is utilized. An examination of the control surface δ response in figure 12 reveals some of the effects of the nonlinearities in the actual electropneumatic servo system. For example, a difference in the characteristics of the control surface motion can be noted between the responses for the positive and negative directions. Some static friction or sluggishness is also apparent for small amplitude control surface motion (note the δ motion between 1.6 and 2.6 seconds). This sluggishness causes a noticeable decrease in the damping of the acceleration response.

Flight-Test Results

Transverse acceleration and δ time histories.- The time histories of the telemetered flight data obtained from the two transverse accelerometer records (c.g. and nose), control surface deflection and qualitative servo valve motion records are shown in figure 14(a). These time histories include a complete pulsing cycle following booster separation, and the conditions correspond closely to the flight conditions and pulsing cycle used for the previous analytical and preflight simulator results. The transverse acceleration responses shown for the first input pulse (3.6 to 4.2 seconds) have larger amplitude oscillations than were expected, and the initial overshoot of the a_{t_0} response is almost as

large as would be obtained in response to a step control surface deflection. An examination of the δ response shown for the initial pulse in figure 14(a) reveals that the control surface motion actually does not deviate greatly from a square wave pattern. The initial rapid control surface motion occurred because the input from the programmer pulsed before the canard unlocking device released. Note that the servo valve motion initiates at 3.6 seconds whereas the control surface motion does not begin until approximately 0.07 second later. The result shown in figure 14(a) is a rapid snap of the control surface to more than 4° before being retarded by the rate feedback signal through the nose accelerometer. Actually the flight record shows a high frequency oscillation (about 45 cps) which accompanies the snapping action of the control surface. Although these oscillations were superimposed on the accelerometer records for about 0.12 second, they were faired through for the presentation in figure 14 since they were apparently forced by the oscillating control surface and are not relevant to the functioning of the acceleration control system.

The flight-test responses shown for the second programmed input (4.2 to 5.2 seconds in fig. 14(a)) exhibit the effectiveness of the rate-feedback signal in damping the airframe motion. A comparison with the response for the previous pulse shows that the initial overshoot is less and that the amplitudes of the steady state oscillations are considerably reduced during the second pulse.

The flight-test responses shown between 5.2 and 6.2 seconds indicate that the canard steadies out at 1° during the final pulse. This control surface deflection results in a steady state value of a_{t_o} between 1.0 and 1.5g instead of the zero values predicted in figures 11 and 12. The two main factors which contribute to the system not trimming at a zero steady state value during the final pulse are: (1) the inability to achieve the exact electrical-mechanical center in balancing the servo system prior to flight test and (2) although the results of reference 1 showed that the steady state error, due to aerodynamic out-of-trim moment, was theoretically zero for the acceleration control system, out-of-trim moments may have a significant effect on the flight-test results, since a physical servo system is being dealt with which could not be expected to integrate out the misalinement errors as perfectly as was implied by the preliminary analysis. The steady state error obtained for the final pulse shown in the flight-test data is noticeable, due to the nature of the programmed command inputs. However, in a homing application this magnitude of unbalance would probably be inconsequential because the input to the control system would be continuously dictated by the guidance or seeker.

Discussion of β and ψ time histories.- The time histories of β and ψ shown in figure 14(b) were obtained from telemetered flight data and the time interval corresponds to the results presented in figure 14(a).

The summation of $\beta + \psi$ is also shown in figure 14(b) since this quantity is a direct measure of the manner in which the yaw flight path angle is changing and is of interest in connection with trajectory studies or homing problems.

The preflight simulator was not constructed so that a direct comparison of the ψ or $\beta + \psi$ time histories could be made since it was desirable to keep the portable electronic analog equipment at a minimum. The yaw attitude ψ time history shown in figure 14(b) may be compared with the theoretical ψ response shown in figure 11. In particular, during the middle pulse, this comparison shows that the manner in which ψ varied with time during the flight test was fairly well predicted by the previous analysis. The variations between theory and experiment may be attributed mainly to the difference in the characteristics and magnitude of the theoretical and physical control surface motion.

Comparison of Flight Test and Preflight Simulator Results

Main variations.- The main variation between the simulator and flight test responses are readily apparent from a comparison of figures 12 and 14(a). The low damping shown for the initial flight-test pulse and the unbalance in the flight data were discussed previously under the heading "Transverse acceleration and δ time histories." Aside from these variations, there are other noticeable differences between the preflight simulator and the flight data which may be enumerated as follows:

1. A comparison between the initial pulses shows the steady state δ to be 3.8° for the simulator result compared with 6° for the flight test, while the steady state transverse accelerations are in approximate agreement.

2. During the second pulse, the steady state δ is 1.3° for the simulator and 2.6° for the flight test, while the steady state a_{t_o} is 5g for the simulator compared with 7.4g for the flight test result.

3. The response to the second pulse shown for the flight data is slower and better damped than the corresponding simulator response.

4. The δ motion during the third flight-test pulse is smoother than the δ motion for the third pulse shown in figure 12. This smoothing out of the δ motion under actual flight-test conditions probably occurs because the servo static friction near zero deflection is alleviated by small-amplitude high-frequency missile vibrations.

Reasons for variations between flight and preflight simulation results.- Part of the variation in steady state values between flight

test and simulator test may be attributed to hinge moment. The hinge moment effect, however, will be discussed in a separate section. Aside from the hinge moment effect and to a certain extent the previously discussed out-of-trim effect, some of the steady state variation noted may be due to nonlinear aerodynamics. For example, using the flight-test steady state values given in the previous section, it may be seen that the steady state relation between a_{t_o} and δ is approximately 2.4 g/deg for the first pulse and 2.8 g/deg for the second pulse whereas a linear relation between these steady state values is obtained with the preflight simulator.

The reduction in the amplitude of the steady state transverse acceleration oscillations and the apparently slower control motion and acceleration response noted for the second flight-test pulse is probably due to the combined effect of several contributing factors. The most significant of these factors are itemized as follows:

(1) The flight-test response obtained for the second pulse is influenced by the end conditions of the first pulse.

(2) The airframe as flight tested was heavier and had correspondingly more inertia than used for the simulated airframe analog.

(3) To a certain extent the variation of Mach number and atmospheric conditions would cause expected variations between flight data and preflight simulation which could not be accounted for beforehand.

(4) Since the pneumatic servo system is not an irreversible system (that is: it is possible for the hinge moment to partially overcome the servo force), the effect of free-floating canards may influence the damping in free flight. (Ref. 6 discusses the effects of free-floating canards.)

Figure 15 shows a calculated response which includes the first two of these items and this response is compared with the response with zero initial values of $\dot{a}_t$ and $\ddot{a}_t$ at the start of the motion. The curve shown for zero initial conditions actually reflects the conditions at the beginning of the second pulse of the preflight simulator results shown previously in figure 12. The block diagram inset at the top of figure 15 illustrates the conditions assumed in obtaining the responses shown. The servo is assumed to be an ideal integration with a gain of 20 chosen to approximate the servo response presented previously in figure 5. The airframe transfer functions ($\ddot{\psi}/\delta$ and $a_{t_o}/\ddot{\psi}$) include the mass and inertia values measured for the model prior to the flight test. The initial values of $\dot{a}_{t_o}$ and $\ddot{a}_{t_o}$, which approximate the end conditions of the first flight-test pulse, were obtained graphically from the flight data. A comparison of the responses in figure 15 reveals a decrease in the overshoots of the

transient oscillations when the initial conditions are included in the solution. Although the responses shown in figure 15 are somewhat slower rising than the previous analytical responses (fig. 11), due to the increased mass and inertia, they are still considerably faster than the flight data; and certainly the presence of initial conditions does not show much of an influence on the rise time. Item (4) of the previous list, however, may have a large influence on the rise time obtained during free flight and should not be overlooked as a possible cause of discrepancies between the predicted and the actual flight-test system behavior.

Effect of hinge moment.- In the previous analytical study (ref. 1), it was shown that the steady state error, due to out of trim or load disturbance (for example, hinge moment), was theoretically zero for an acceleration control system with an integration in the forward loop. In other words, regardless of the hinge moment, an input signal calling for 15g must produce a steady state acceleration of exactly 15g. For the physical system, however, this was not the case as can be seen in figure 16. In this figure the results of a preliminary simulator study are presented to show a comparison between the system response with a simulated hinge moment of approximately 6 in-lb per deg δ and the system response for identical conditions except that the servo hinge moment is removed. The variation between the load and no load cases of figure 16 indicate that hinge moment is at least partially responsible for disagreement between flight test and preflight simulation. The initial pulse of figure 16 shows that with the hinge moment removed, the steady state a_{t_o} is about 22g or an increase of 7g over the steady state value obtained with the simulated load applied. The δ responses shown for the initial pulse on figure 16 show an increase of almost 2° when the external load is removed. The increase in a_{t_o} and δ steady state obtained with the hinge moment removed is indicative of the fact that the pneumatic servo does not maintain a perfect integration in the forward control loop. Actually, the servo functions somewhat like a torque servo (see ref. 7), since the final control deflection is not only dependent on the magnitude of the command but is also a function of the balance of an external spring (hinge moment) and an internal spring (sponginess within the piston chamber, due to compressibility and valve leakage). For large control surface deflections, the servo is actually approaching a state of force saturation. An additional servo nonlinearity is apparent when the first and second pulse of figure 16 are compared. This comparison shows that the steady state δ under loaded conditions is 2/3 of the steady state δ with no load for the first pulse; while for the second pulse, the steady state δ is decreased to less than half when the load is applied. A corresponding variation between the a_{t_o} responses for the first and second pulse shown on figure 16 can be noted.

The results shown in figure 16 are significant in that they help to point out the actual nonlinearities present in the physical servo. However, regardless of these nonlinearities the flight data shown previously

in figure 13 do substantiate that the control system is capable of functioning in a prescribed manner to change the missile acceleration from one steady value to some other steady value. In a homing application, when the input to control system is continuously dictated by the seeker, the significance of nonlinearities in the servo system will probably not be important as long as the missile responds to the seeker inputs to turn in the direction of the target.

CONCLUDING REMARKS

The maneuvers obtained during flight confirm satisfactory control system operation and it is significant that the system is applicable to some present-day missiles which utilize linear acceleration commands as a means of rotating the flight path vector to reduce navigation errors. The flight-test results also show that the method employed to obtain yaw-rate feedback is effective in augmenting the damping of the airframe motion during an acceleration command maneuver.

The control elements used in this flight-test investigation are considered to be relatively simple and their physical arrangement is probably unique to the missile application. For example, the effect of integration is obtained in the servo loop by the introduction of the proper passive electrical network and this integrating servo is combined with angular acceleration feedback to provide the equivalent of angular-rate feedback damping without using a rate gyroscope.

A comparison of the preflight simulation results with the preliminary analytical results shows favorable agreement except that the simulated transverse acceleration transient response is more oscillatory in approaching steady state. This result was attributed to variations between the physical servo and its ideal representation as used for the preliminary analysis. Several nonlinearities in the electropneumatic servo system were evidenced by the simulation and flight-test results. Comparisons between flight data and preflight simulation results were further complicated by airframe nonlinearities and other variations between the physical airframe and its electronic analog. Nevertheless, the flight data substantiate that the control system is capable of functioning in a prescribed manner to change the missile acceleration from one steady value to some other steady value.

Langley Aeronautical Laboratory,
National Advisory Committee for Aeronautics,
Langley Field, Va., August 2, 1955.

REFERENCES

1. Seaberg, Ernest C., and Smith, Earl F.: Theoretical Investigation of an Automatic Control System With Primary Sensitivity to Normal Accelerations as Used to Control a Supersonic Canard Missile Configuration. NACA RM L51D23, 1951.

2. Anon: Guided Missile System, XSAM-A-7. Missile and Booster. Missile Guidance Section, GS-15660 - Maintenance Notes, Vol. II. Bell Telephone Labs., Inc. (U. S. Army Ord. Corps Contract W30-069-ORD-3182), Rev. Oct. 15, 1953.

3. Zarovsky, Jacob, and Gardiner Robert A.: Flight Investigation of a Roll-Stabilized Missile Configuration at Varying Angles of Attack at Mach Numbers Between 0.8 and 1.79. NACA RM L50H21, 1951.

4. Chestnut, Harold, and Mayer, Robert W.: Servomechanisms and Regulating System Design. Vol. I. John Wiley & Sons, Inc., 1951, p. 319.

5. Gardiner, Robert A., and Zarovsky, Jacob: Rocket-Powered Flight Test of a Roll-Stabilized Supersonic Missile Configuration. NACA RM L9K01a, 1950.

6. Curfman, Howard J., Jr., Strass, H. Kurt, and Crane, Harold L.: Investigations Toward Simplification of Missile Control Systems. NACA RM L53I21a, 1953.

7. Blaise, Robert A.: Report of Flight Tests of SIDEWINDER (EX-0) Missiles 1X, 2X, 3X, and 4X. NOTS TM 273, U. S. Naval Ord. Test Station (Inyokern, Calif.), Oct. 10, 1952.

TABLE I

SERVOMOTOR PHYSICAL CHARACTERISTICS

Length of piston stroke, in.	0.42
Cylinder overall length, in.	1.75
Effective piston area, sq in.	0.34
Operating pressure, lb/sq in.	150
Weight, oz	14

TABLE II

ACCELERATION CONTROL MISSILE PHYSICAL CHARACTERISTICS

I_Z, slug-ft^2	41
I_Y, slug-ft^2	41
I_X, slug-ft^2	1.2
Center-of-gravity location, in. from station zero	73.8
Center-of-pressure location at $M = 1.6$, in. from station zero	79.8
Distance between nose accelerometer and c.g., ft	5.5
Model weight, lb	190
Overall model length, in.	130
Fuselage diameter, in.	8
Total wing area in one plane, sq ft	4.1
$\bar{c}$, ft	1.776

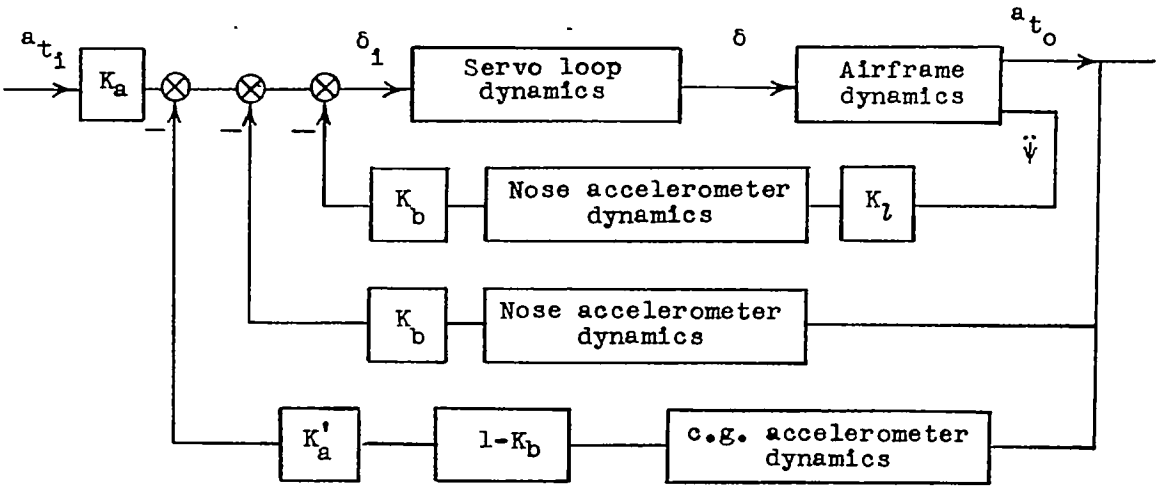

(a) Complete representation.

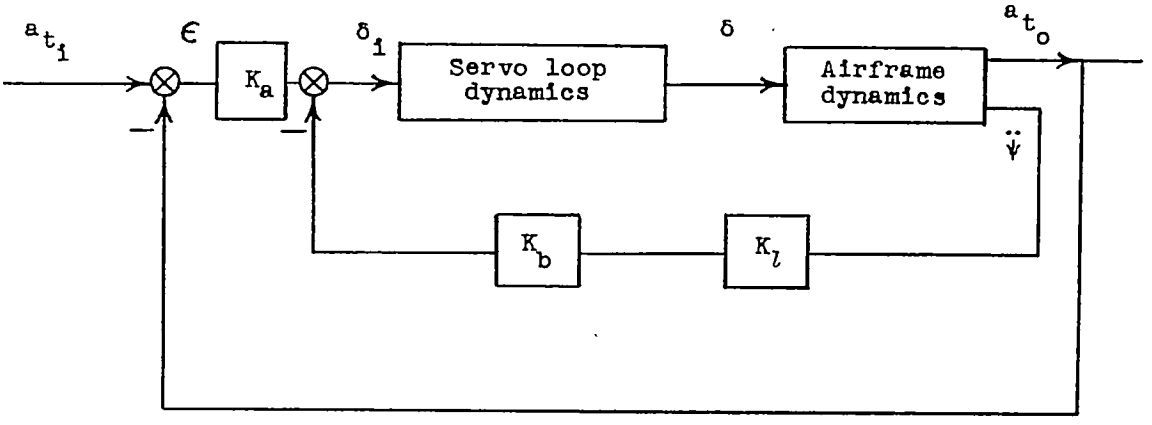

(b) Simplified representation.

Figure 1.- Functional diagrams of a transverse acceleration control system.

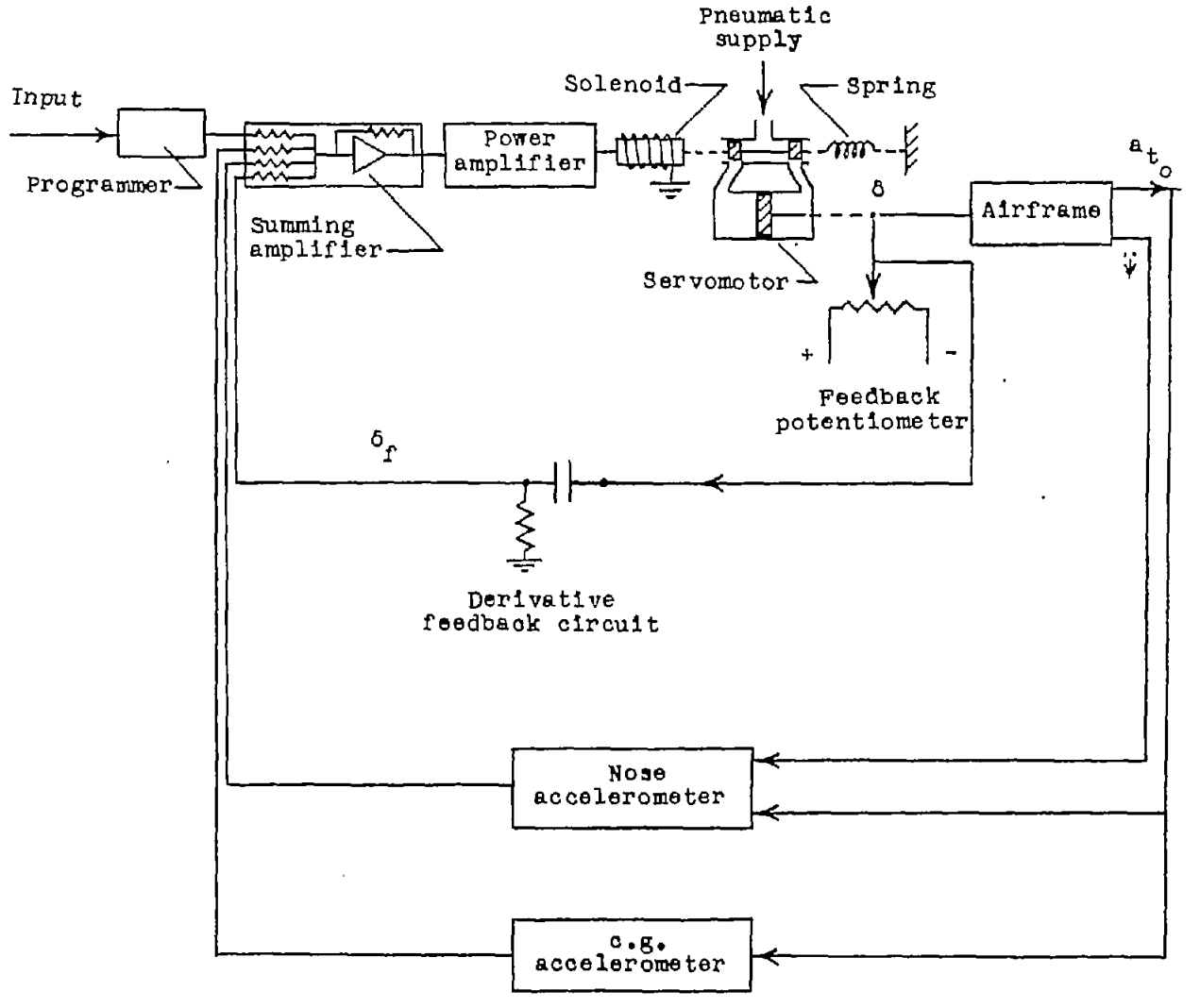

Figure 2.- Block diagram of acceleration control system with the servo loop represented schematically.

CONFIDENTIAL

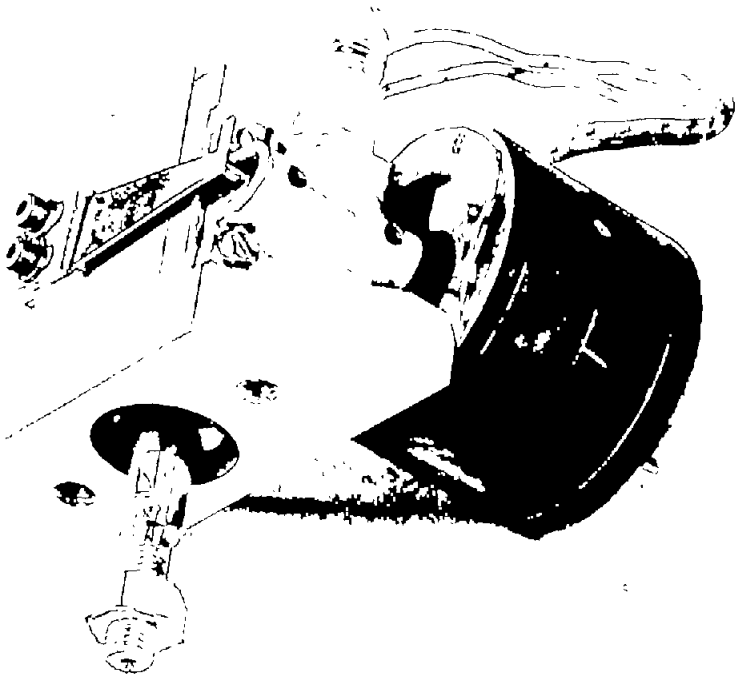

L-87611

Figure 3.- Photograph of control system servomotor including spring and solenoid.

CONFIDENTIAL

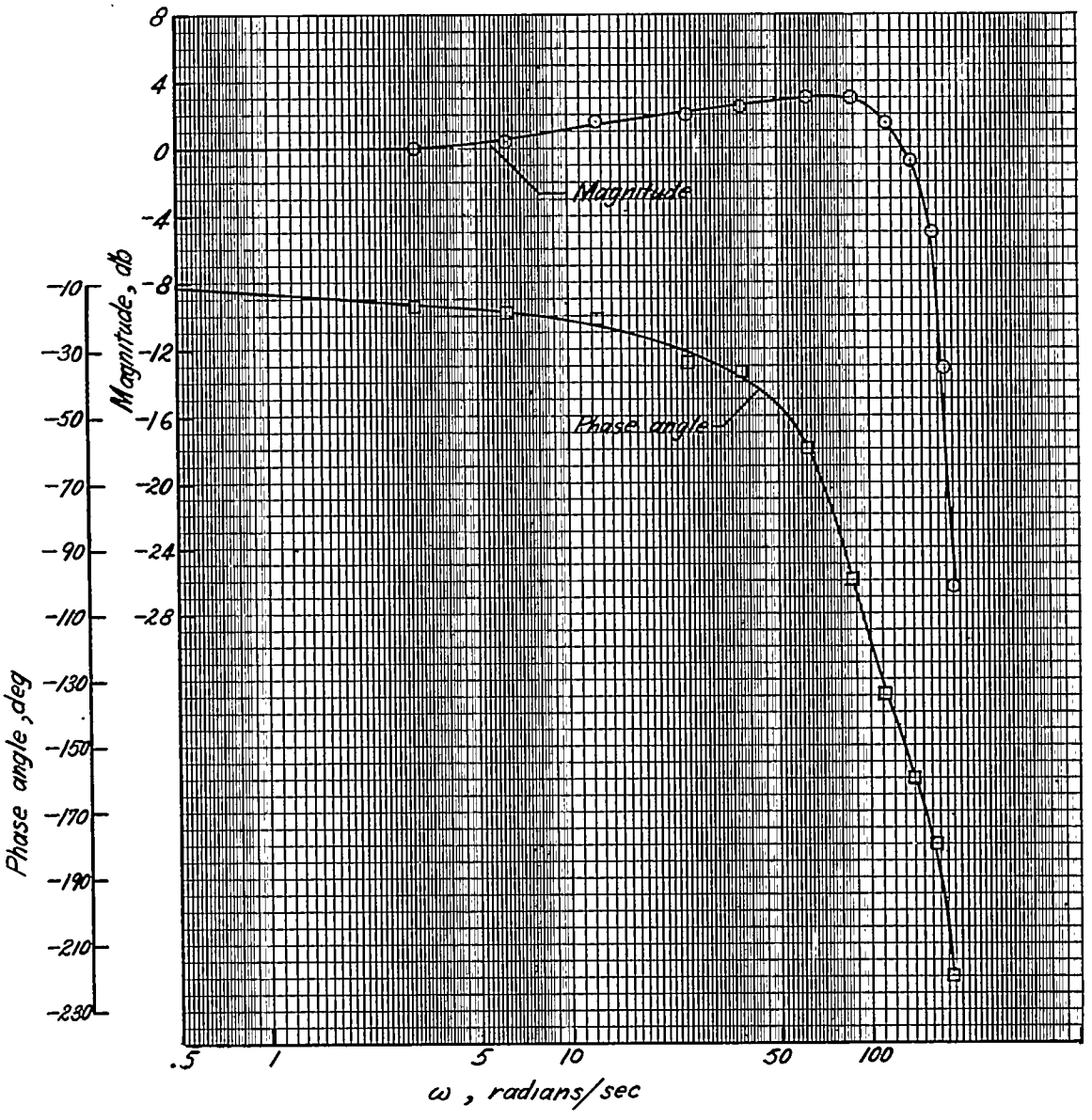

Figure 4.- Measured frequency response of servo elements with unity position feedback. Sinusoidal input voltage = ±3.3 volts.

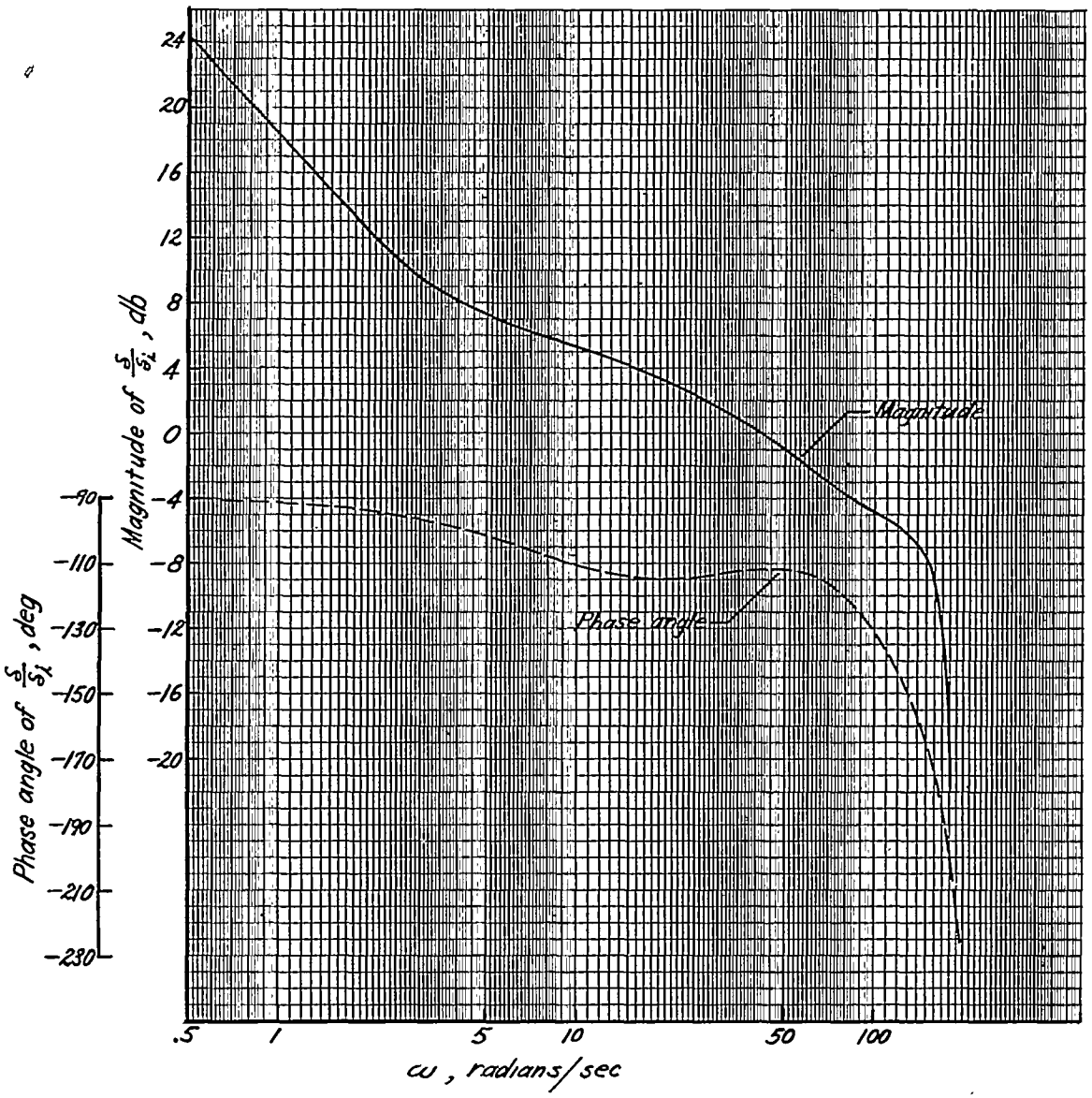

Figure 5.- Approximation of servo loop frequency response $\frac{\delta}{\delta_i}$ including derivative feedback (τ = 0.01 sec).

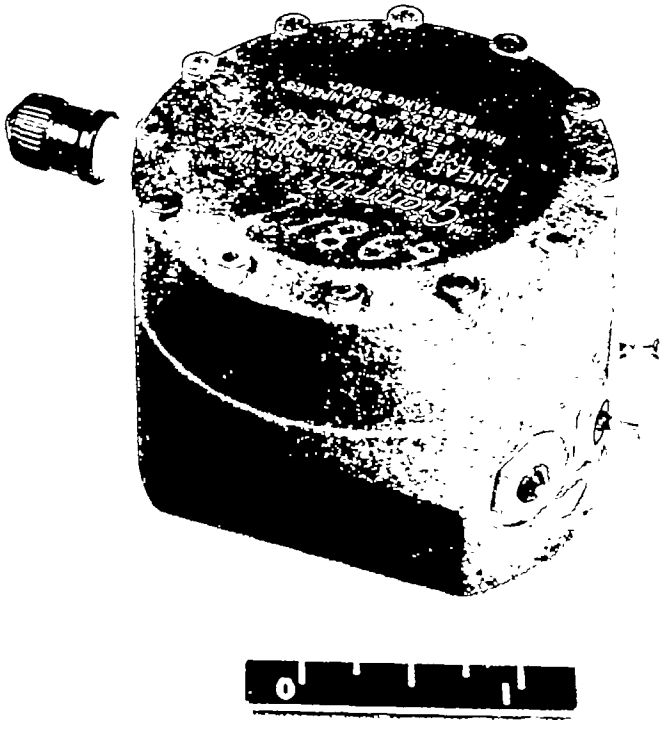

L-87497

Figure 6.- Photograph of control system accelerometer.

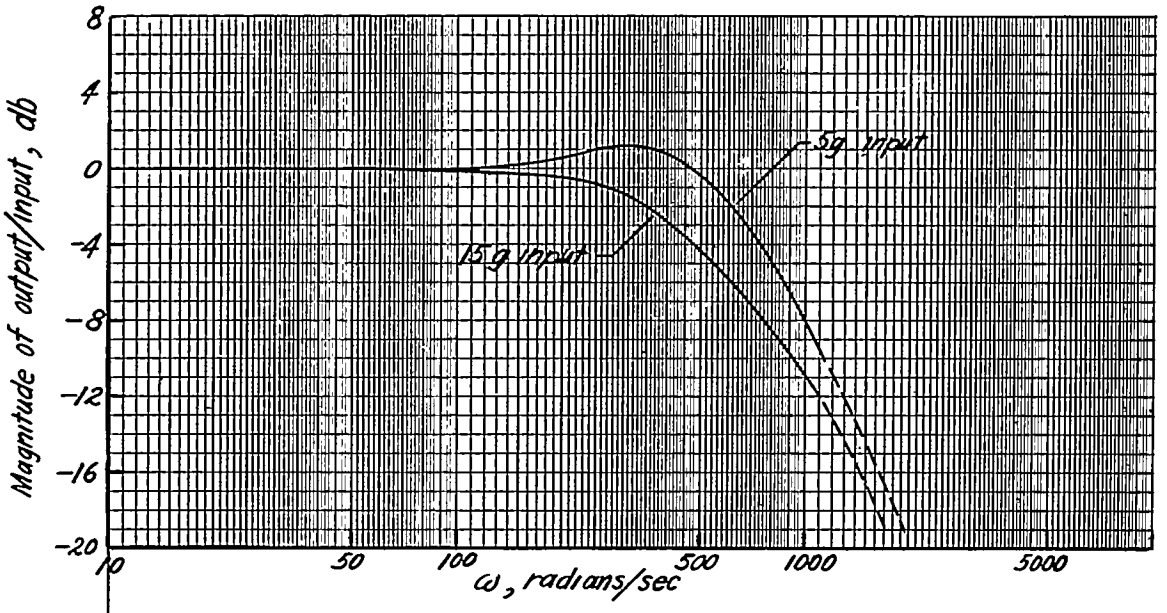

(a) Nose accelerometer.

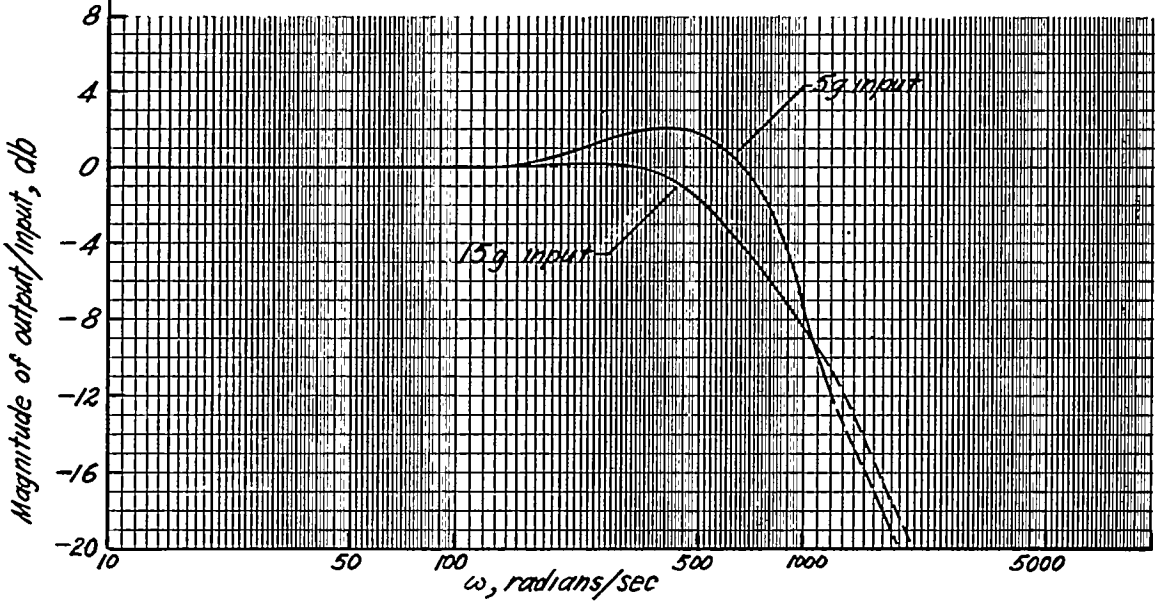

(b) Center-of-gravity accelerometer.

Figure 7.- Nose and center-of-gravity accelerometer amplitude responses as determined from laboratory measurement.

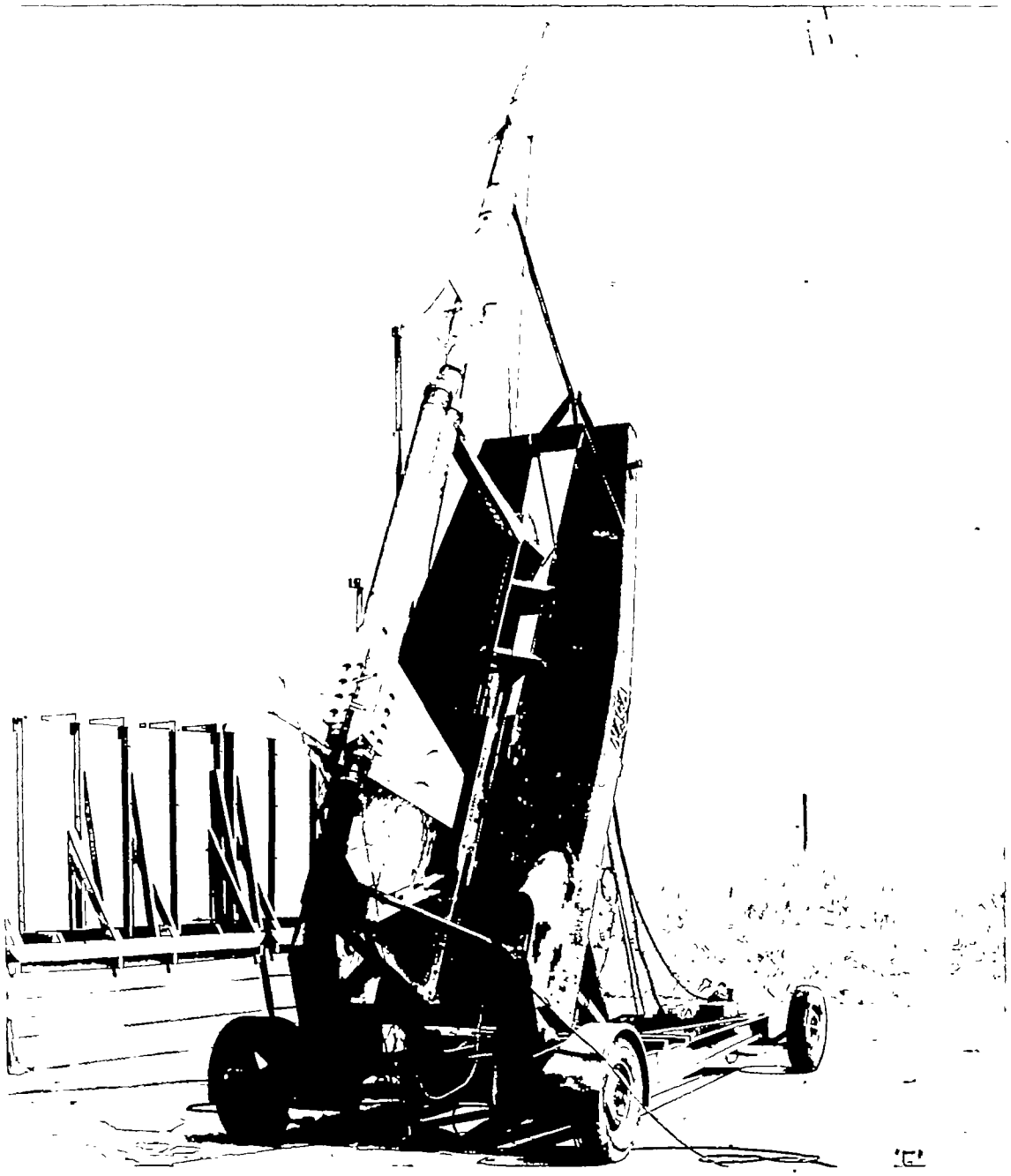

L-86322.1

Figure 8.- Photograph of model and booster on launcher.

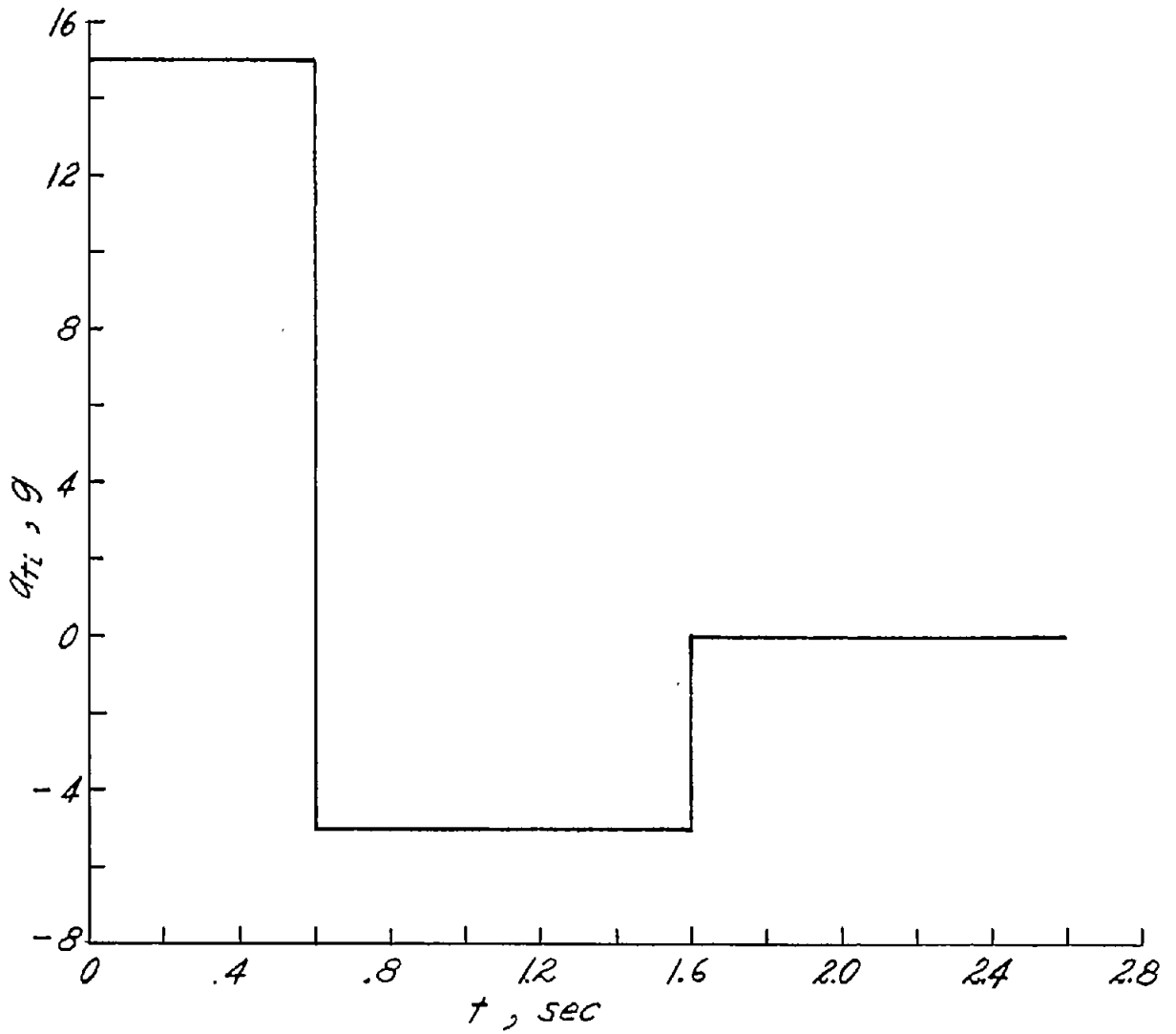

Figure 9.- Sequence of programmed input commands.

CONFIDENTIAL

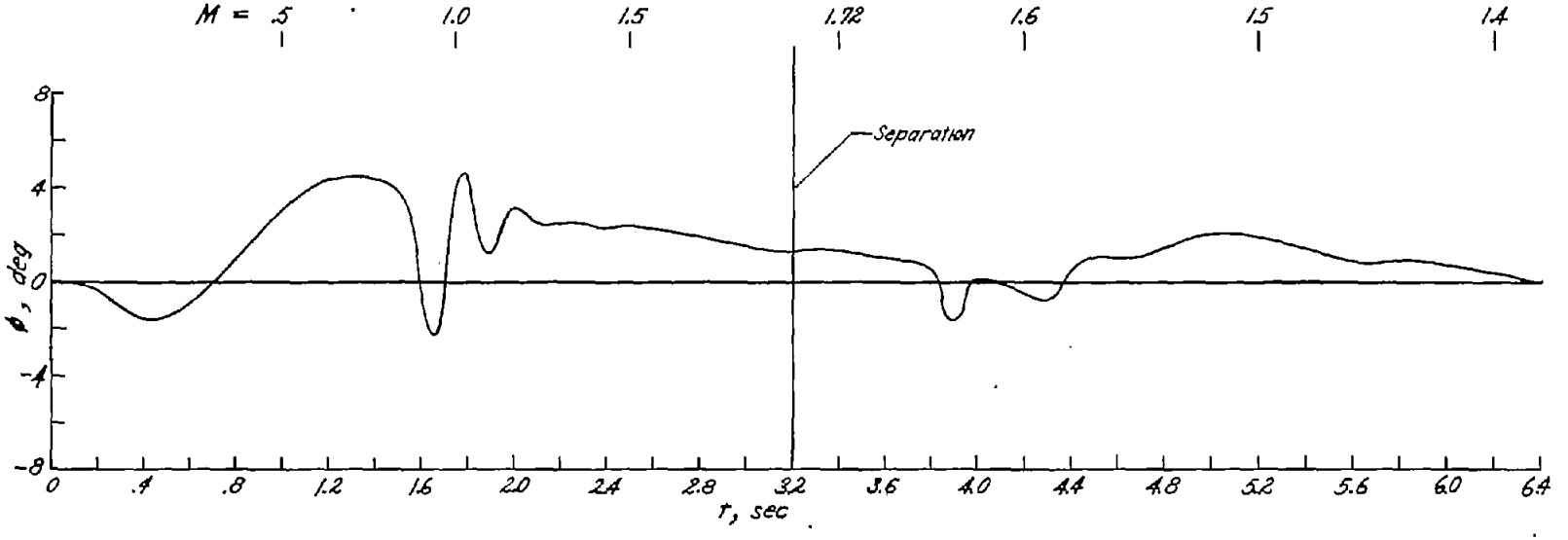

Figure 10.- Time history of bank angle ϕ obtained from telemetered flight data.

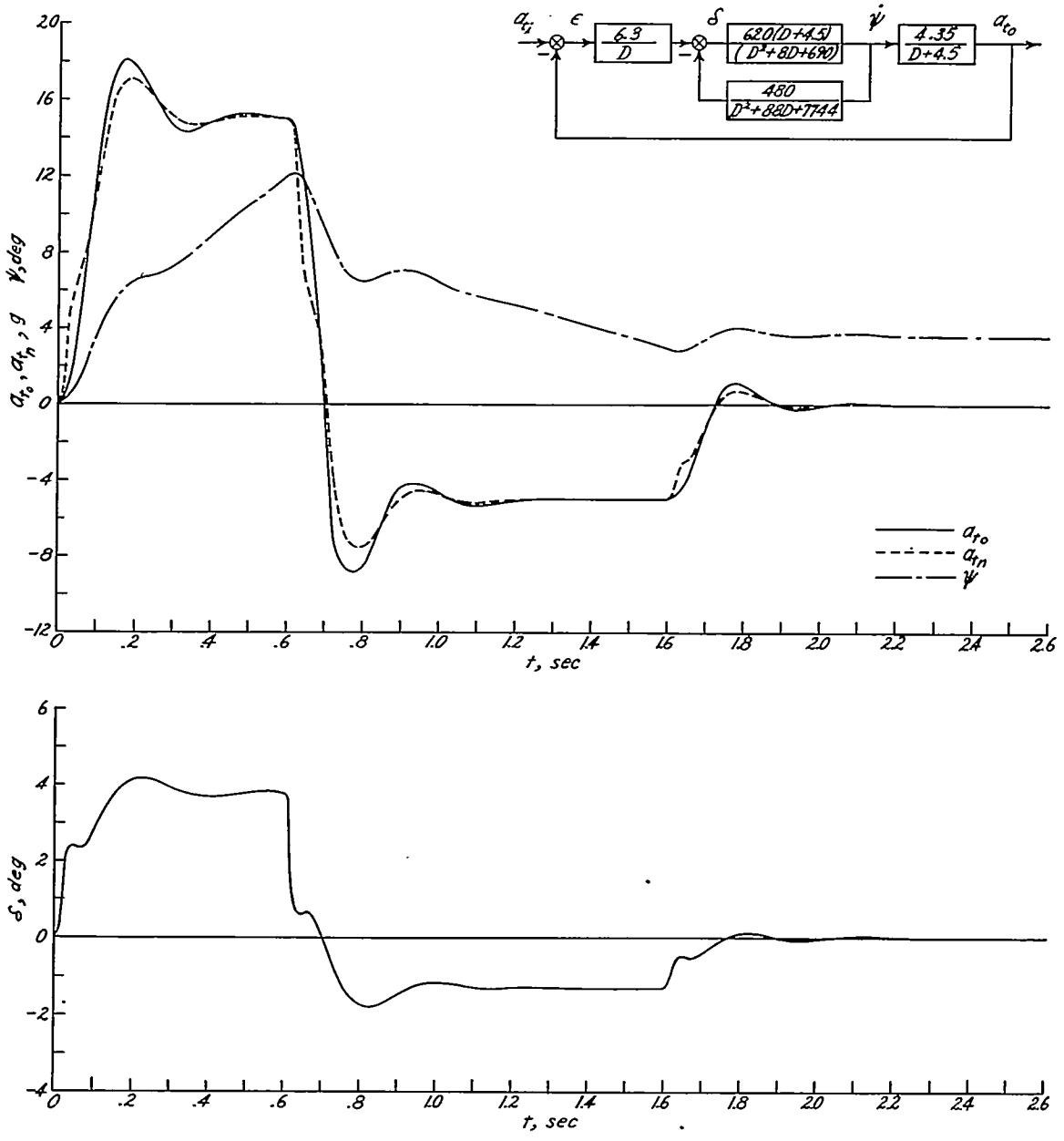

Figure 11.- Theoretical prediction of the flight test responses to a programmed sequence of command inputs equivalent to 15g, -5g, and 0g, respectively. These predictions are based on the analytical data presented in reference 1 for sea-level flight at $M = 1.6$ with $x_{sm} = 0.294\bar{c}$, and the rate gyroscope dynamics included in the inner feedback loop is shown above.

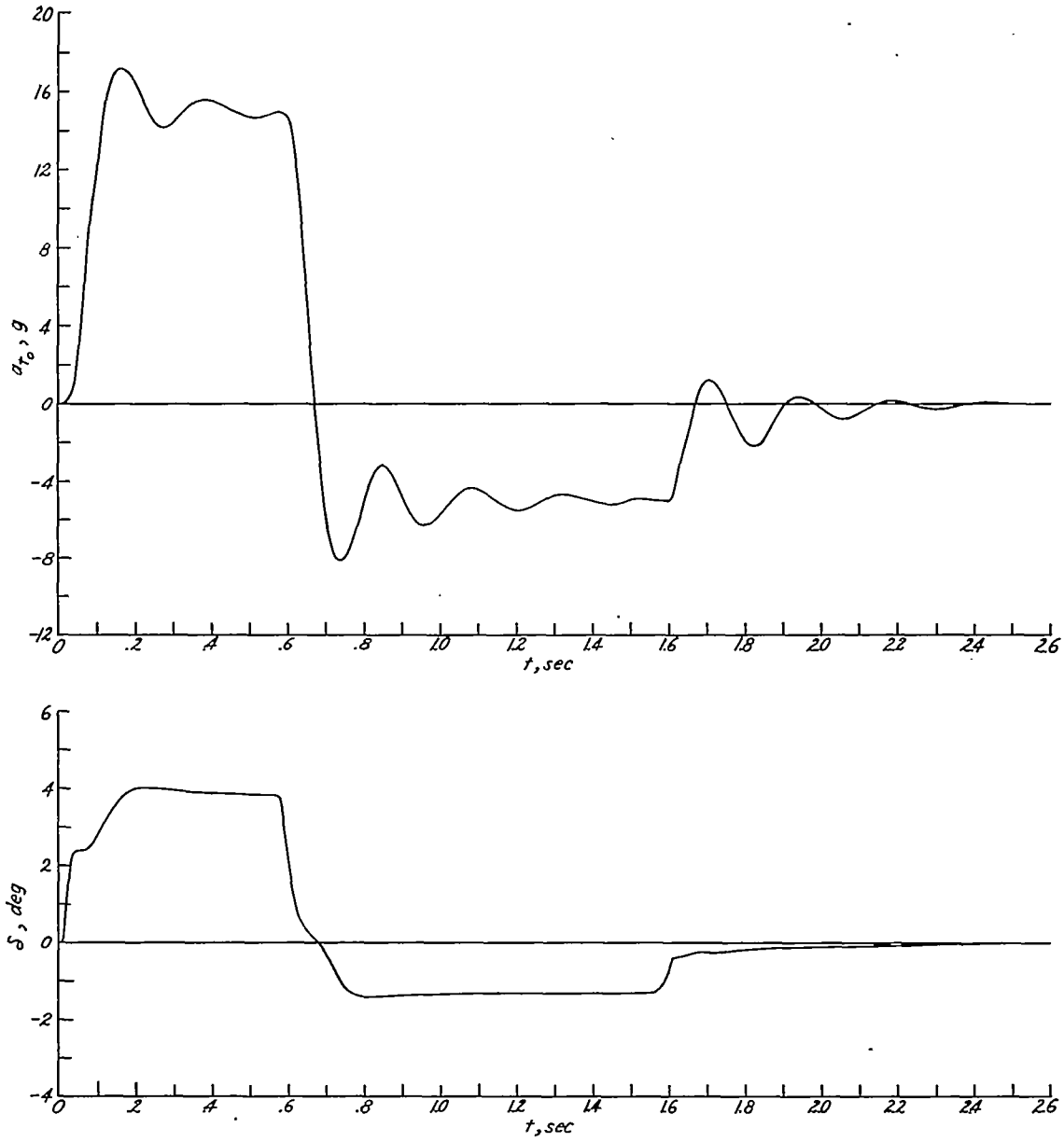

Figure 12.- Electronic preflight simulator result obtained prior to flight test with the airframe transfer function simulated for sea-level flight at $M = 1.6$ with $x_{sm} = 0.294\bar{c}$. Approximate canard hinge moment = 6 in-lb per deg; $K_b = 0.616$ volt/g; $K_a = 0.136$ volt/g.

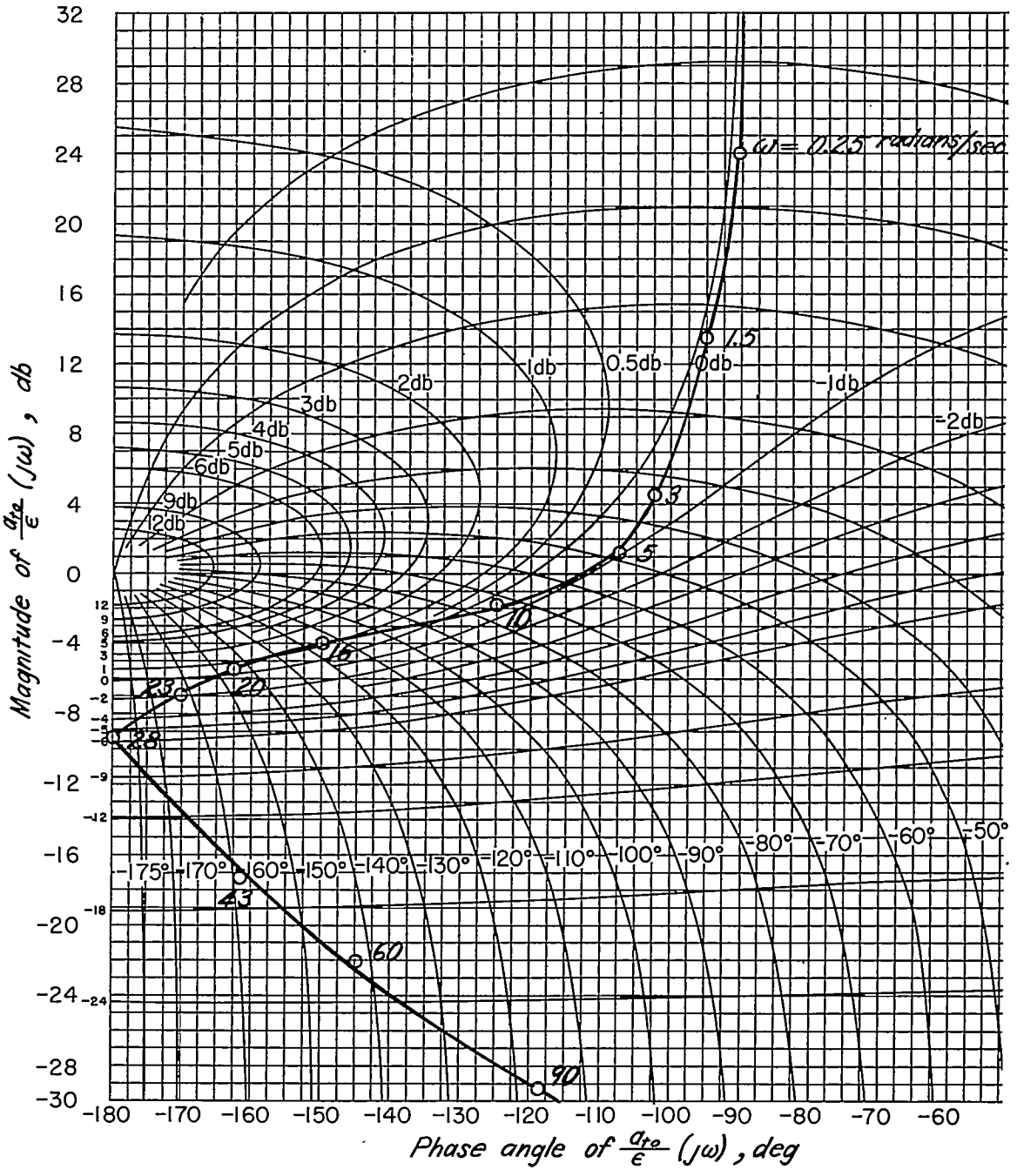

Figure 13.- Nichols chart showing frequency response corresponding to final preflight simulator conditions with servo loop represented graphically as in figure 5. K_b = 0.616 volt/g; K_a = 0.136 volt/g; K_l = 0.003 g/deg/sec^2.

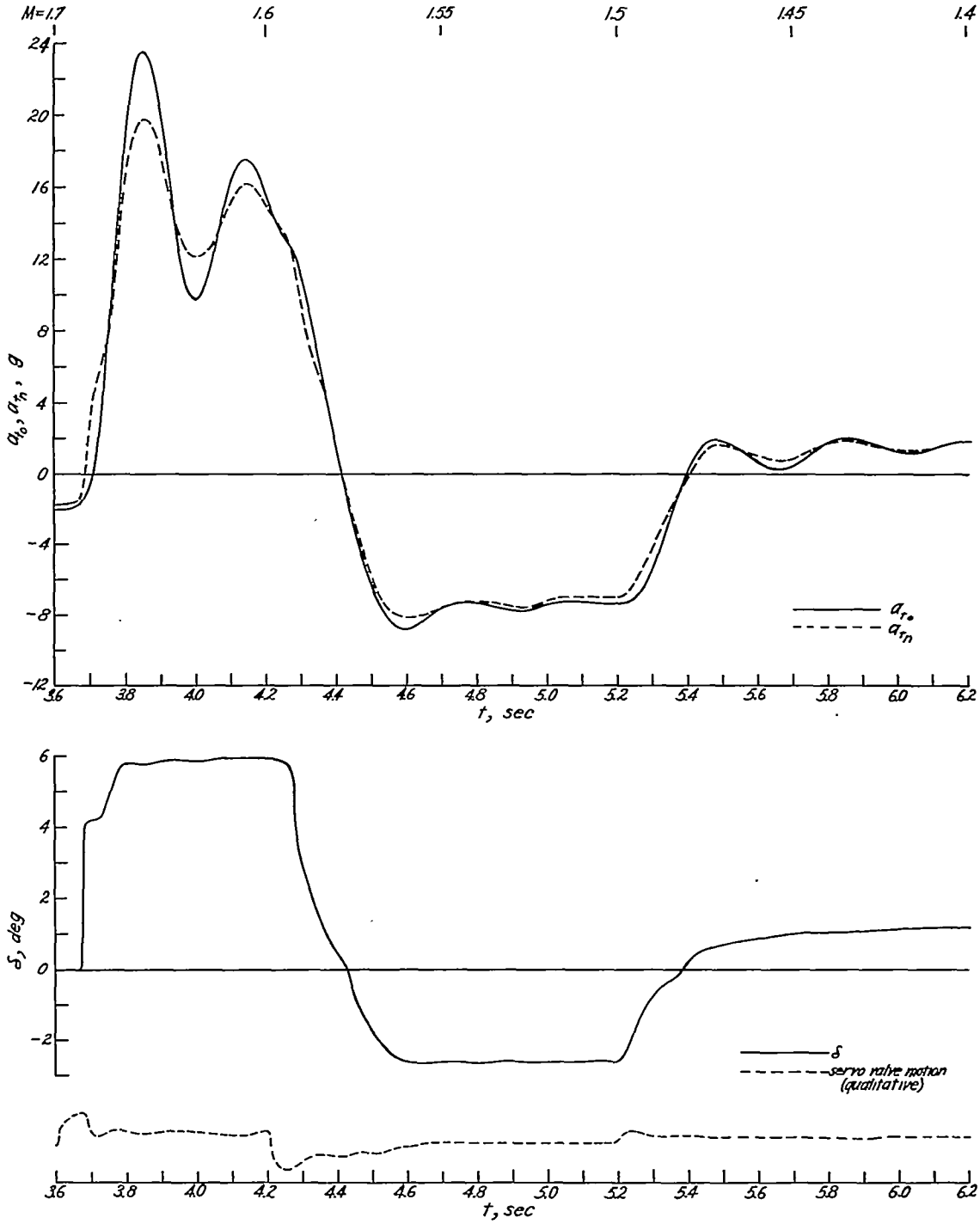

(a) a_t, δ, and servo valve motion.

Figure 14.- Time histories of flight test responses to programmed command inputs obtained from telemeter data.

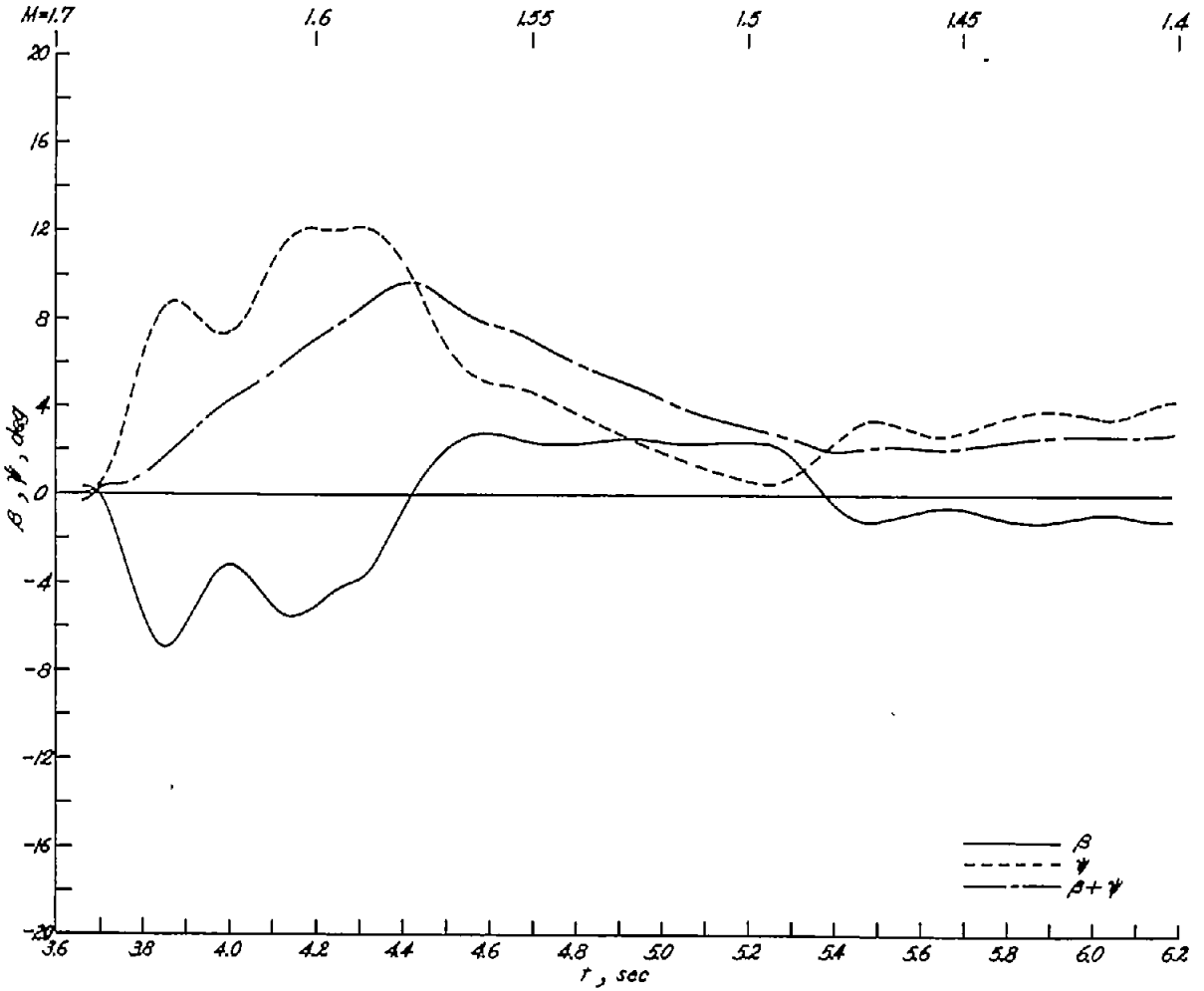

(b) β, ψ, and β + ψ.

Figure 14.- Concluded.

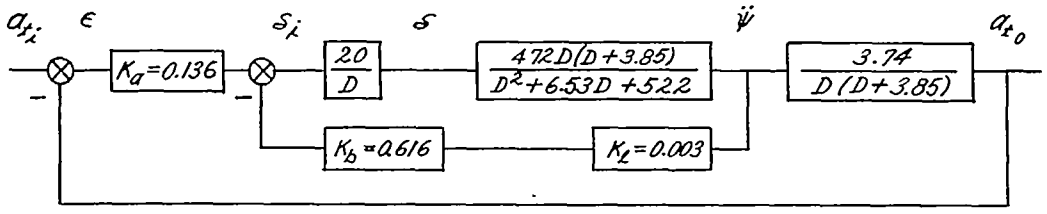

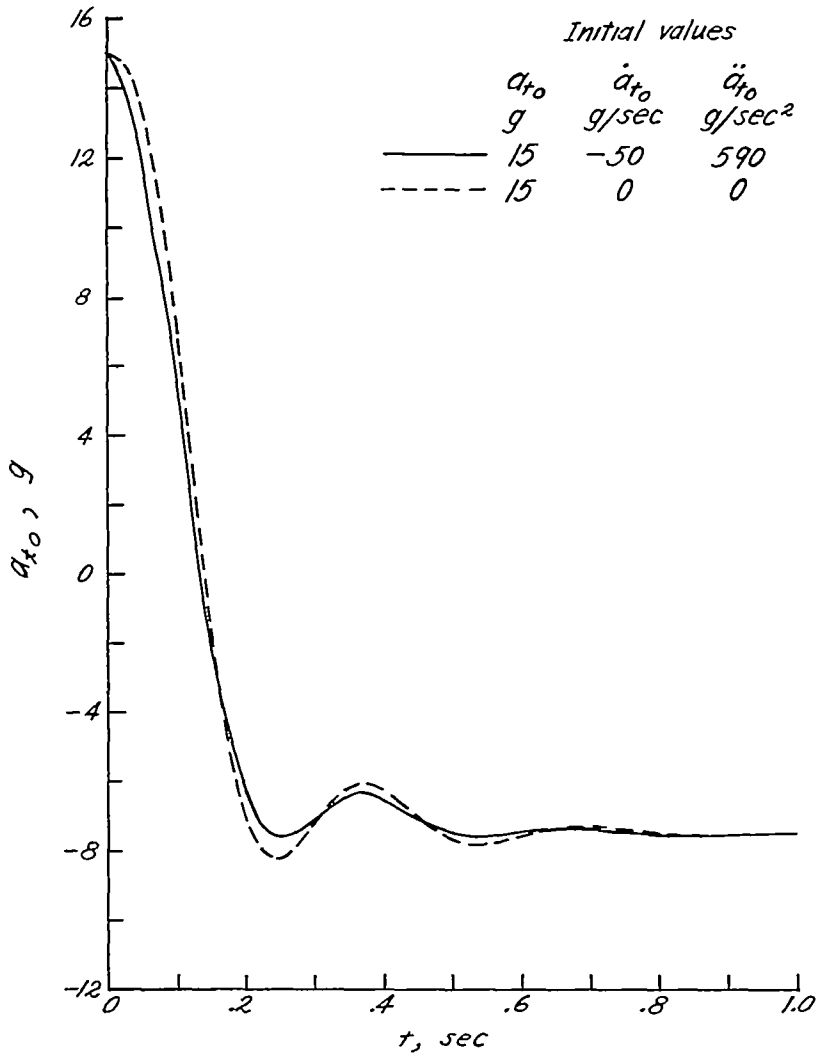

Figure 15.- Calculated responses to a command input calling for a change in a_{t_o} from +15g to -7.5g showing the difference between the response including initial values of $\dot{a}_{t_o}$ = -50g/sec and $\ddot{a}_{t_o}$ = 590g/sec^2 and the response for which these initial values are zero. The initial values used in computing the solid curve approximate the conditions existing at the start of the second flight test pulse.

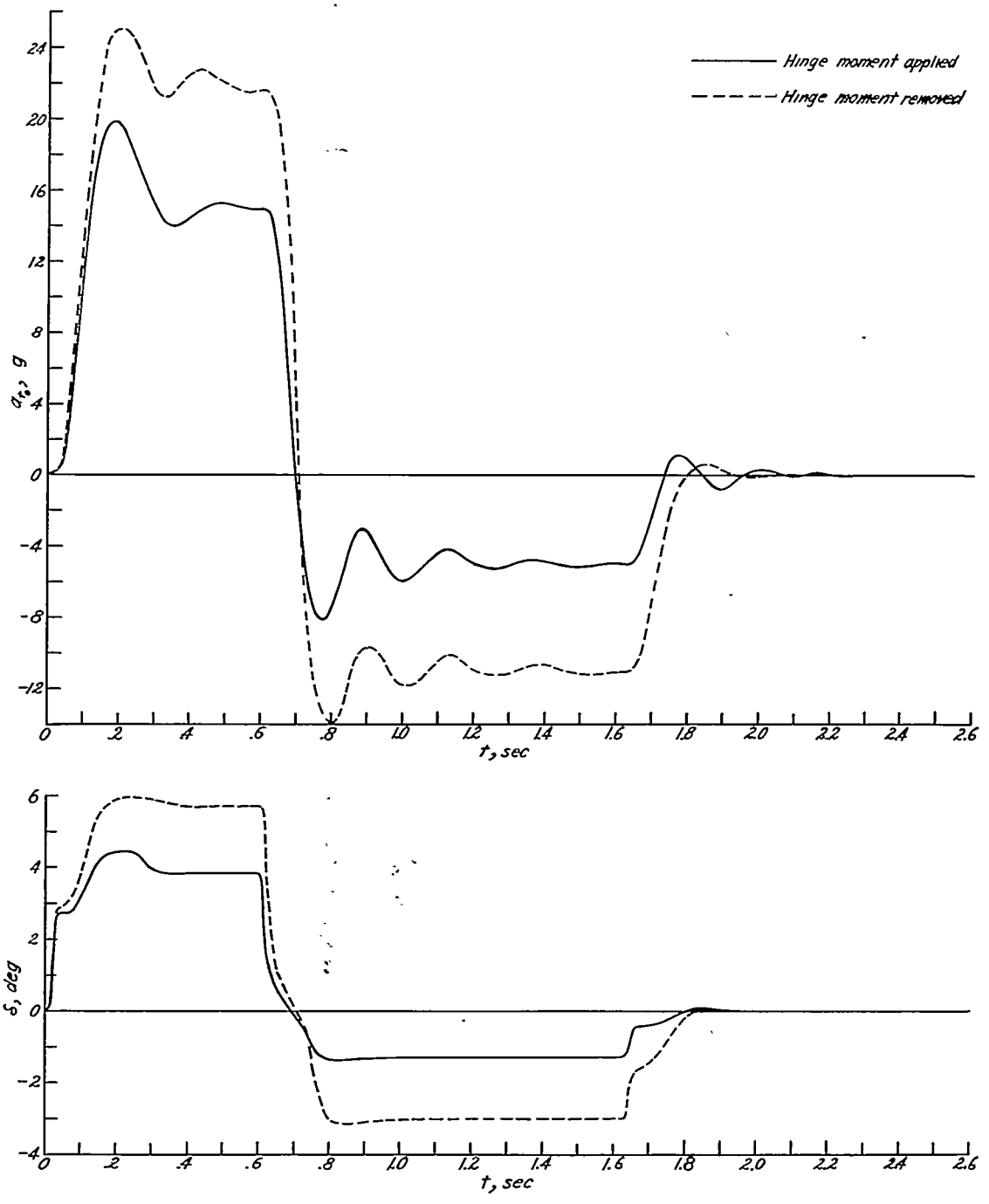

Figure 16.- Preflight simulator response obtained with a servo hinge moment of approximately 6 in-lb per degree canard deflection compared with the preflight simulator response obtained for identical conditions except that the servo hinge moment is removed.

NACA - Langley Field, Va.